Locating End-Effector Tips in Robotic Micromanipulation

Jun Liu, Zheng Gong, Kathryn Tang, Zhe Lu, Changhai Ru, Jun Luo, Shaorong Xie, and Yu Sun

***Abstract*—In robotic micromanipulation, end-effector tips must be first located under microscopy imaging before manipulation is performed. The tip of micromanipulation tools is typically a few micrometers in size and highly delicate. In all existing micromanipulation systems, the process of locating the end-effector tip is conducted by a skilled operator, and the automation of this task has not been attempted. This paper presents a technique to automatically locate end-effector tips. The technique consists of programmed sweeping patterns, motion history image end-effector detection, active contour to estimate end-effector positions, autofocusing and quad-tree search to locate an end-effector tip, and, finally, visual servoing to position the tip to the center of the field of view. Two types of micromanipulation tools (micropipette that represents single-ended tools and microgripper that represents multiended tools) were used in experiments for testing. Quantitative results are reported in the speed and success rate of the autolocating technique, based on over 500 trials. Furthermore, the effect of factors such as imaging mode and image processing parameter selections was also quantitatively discussed. Guidelines are provided for the implementation of the technique in order to achieve high efficiency and success rates.**

***Index Terms*—Autofocusing, end-effector detection, locating end-effector tips, robotic micromanipulation.**

I. Introduction

Micromanipulation tools such as micropipettes and microelectromechanical systems (MEMS) microgrippers are commonly used in the manipulation of microscaled objects. Locating the tip of these end-effectors under microscopy must be conducted before micromanipulation initiates. In present manual and robotic micromanipulation, locating the tip of end-effectors (searching, positioning, and focusing) is presently a manual procedure performed by skilled operators. Because of the small size and fragility of micromanipulation end-effectors, manually locating end-effector tips has high skill requirements, is time consuming, and can cause end-effector breakage. Despite the progress made in robotic micromanipulation [1]–[5], the automation of the procedure of locating end-effector tips has not been investigated.

Most end-effectors used in micromanipulation have micrometer-sized tips (single or multiended). For instance, micropipette tips used in cell manipulation and microgrippers for assembly tasks are usually a few micrometers in diameter (see Fig. 1). The tiny tip of these end-effectors is difficult to locate, particularly under high magnifications in microscopy imaging. When the end-effector collides into other objects (e.g., wafer substrate, glass slide, petri dish, or other end-effectors) during the process of locating the end-effector and micromanipulation, the tip can be easily damaged and requires replacement. Hence, automation techniques to readily locate the end-effector tips are necessary to reduce human intervention and achieve autonomous robotic micromanipulation.

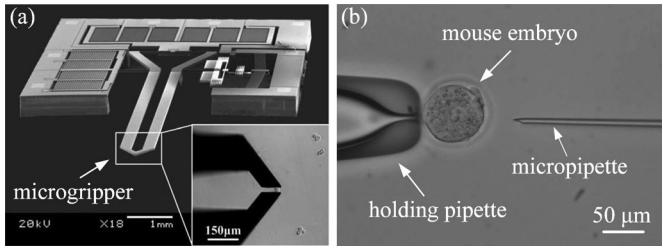

Fig. 1. Example end-effectors used in micromanipulation. Their micrometer-sized tips must be located first before micromanipulation initiates. (a) Microgrippers for pick–place of small objects. The grasped particles are 10 μm in diameter. (b) Micropipettes for manipulating biomaterials.

Automatically locating end-effectors requires visual detection and focus estimation to determine the end-effector's position in three dimensions. Several techniques have been reported to visually detect and track microobjects. Ni *et al.* proposed an iterative closest point algorithm to track a microgripper's position [6]. The algorithm requires the use of an additional dynamic vision sensor (silicon retina). This special hardware requirement makes the algorithm unsuitable for micromanipulation tasks that rely on standard vision systems. Microgrippers with complex features were also tracked using the template matching method for microassembly tasks [7], [8]. Our experimental results indicate that the template matching is ineffective to track objects without distinct features (e.g., micropipettes). In another related work [9], a generalized Hough transform was applied to detect end-effector tips. However, the approach can only detect objects with regular shapes (i.e., lines or circular shapes). Algorithms based on one-class support vector machines [10], shearlet multiscale directional transform [11], and the Kalman filter [12] have also been used to detect or track objects under microscopy imaging. However, these algorithms are only suitable to process in-focus images. In the task of locating end-effector tips, the end-effector often is partially or entirely out of focus. In addition, the shapes and end-effectors' direction of entering the field of view (FOV) also vary with different micromanipulation tasks. These unique requirements call for the development of techniques to automatically locate end-effectors under microscopy.

This paper presents a technique that is capable of searching for out-of-FOV, out-of-focus, and low-contrast end-effectors. A detection algorithm based on a motion history image (MHI) and an active contour model is used to search for the end-effector. Through estimating the end-effector tip's location and the use of an adaptive quad-tree autofocusing algorithm, the tip of the end-effector is detected and moved to the center of the FOV and brought in focus. Based on our IEEE ICRA conference paper [13], this paper describes in more detail algorithm comparisons and experimental results. Micropipettes and MEMS microgrippers are used as example end-effectors to evaluate the performance of the technique. Experimental results from the over 500 trials under three common imaging modes (bright field, differential interference contrast or DIC, and phase contrast) demonstrate that the technique is capable of automatically locating end-effectors under microscopy imaging with high efficiency and accuracy.

II. System Design

A. System Architecture

As shown in Fig. 2, the micromanipulation system setup consists of a standard inverted microscope (TE2000-S, Nikon) with motorized

Manuscript received April 3, 2013; revised July 22, 2013; accepted August 25, 2013. Date of publication September 6, 2013; date of current version February 3, 2014. This paper was recommended for publication by Associate Editor A. Ferreira and Editor B. J. Nelson upon evaluation of the reviewers' comments. This work was supported by the Natural Sciences and Engineering Research Council of Canada, the Canada Research Chairs Program, and the Ontario Genomics Institute.

The authors are with Department of Mechanical and Industrial Engineering, University of Toronto, Toronto, ON M5S 3G8, Canada (e-mail: ljun@mie.utoronto.ca; zgong@mie.utoronto.ca; kathryn.tang@utoronto.ca; zhe.lu@utoronto.ca; rchhai@gmail.com; luojun@shu.edu.cn; srxie@shu.edu.cn; sun@mie.utoronto.ca).

Color versions of one or more of the figures in this paper are available online at http://ieeexplore.ieee.org.

Digital Object Identifier 10.1109/TRO.2013.2280060

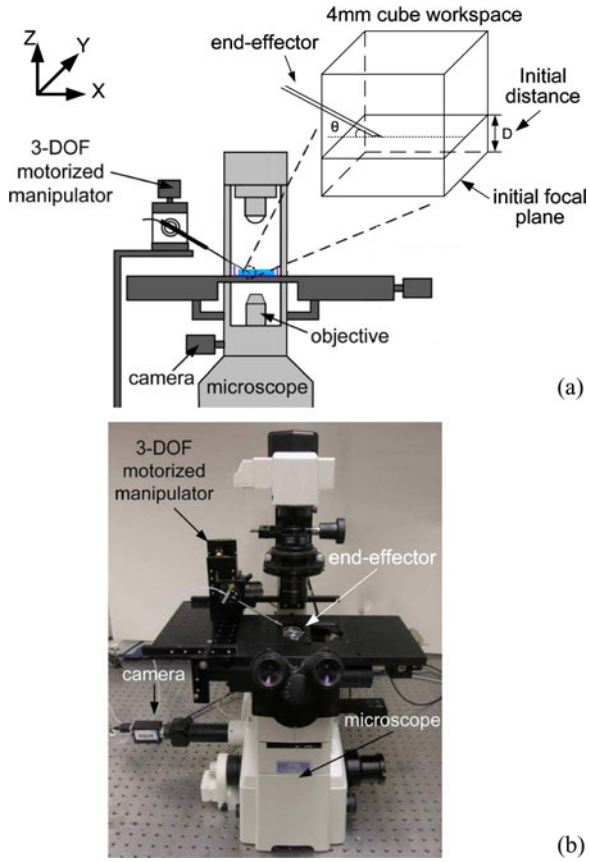

Fig. 2. System architecture (a) Schematic illustration. (b) System picture.

focus control and a CMOS camera connected (scA1300-32gm, Basler; resolution: 1200 × 900). Objectives of 4×, 10×, and 20× are used and have depths of field of 55.5, 13.5, 5.5 μm, respectively. An end-effector (i.e., a micropipette or a microgripper in this study) is mounted on a motorized 3-DOF micromanipulator (Sutter MP285) at a tilting angle of 30°. Movements performed in the automation procedure consist of X, Y, and Z translation motions of the end-effector as well as adjustment of the microscope's focus.

B. Overall Sequence

The end-effector is initially at or above the focal plane. The search range is established within a 4-mm cube of workspace (-2 mm $\leq x \leq +2$ mm, -2 mm $\leq y \leq +2$ mm, 0 mm $\leq z \leq +4$ mm) [see Fig. 2(a)]. When setting up an end-effector in micromanipulation, it is feasible for the operator to readily position the end-effector tip to within this 4-mm cube workspace with unaided eyes and reasonable care.

The automated procedure has two main steps: end-effector detection and autofocus adjustment. Fig. 3 summarizes the overall sequence.

1) End-Effector Detection: In the detection step, the end-effector is swept in the *X–Y* plane. An algorithm based on an MHI is used to detect the presence of end-effector in the FOV. In some cases, the end-effector cannot be detected when it is far away from the focal plane. When this occurs, the focal plane is moved upwards, and horizontal *X–Y* sweep is repeated. The step size of focus adjustment depends on the depth of field of the microscope objectives. In our system, the step size for 4×, 10× and 20× objectives is set as 50, 10, and 5 μm, respectively. When a moving object is detected in multiple continuous frames of

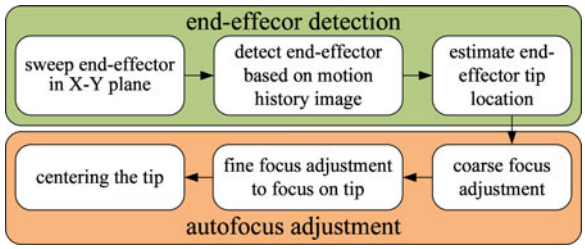

Fig. 3. Overall sequence to locate end-effector tips.

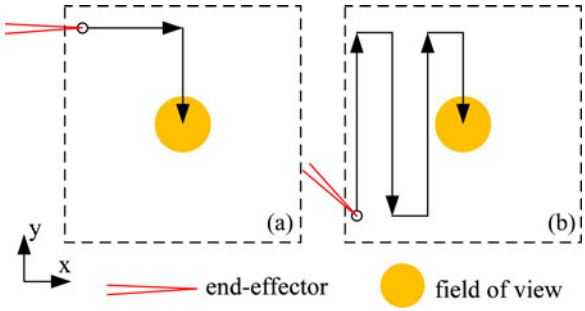

Fig. 4. Sweep pattern in *X–Y* plane (top-down view). (a) When the direction of entering the FOV is known, end-effector is moved along the direction from which it enters the FOV, followed by sweeping perpendicularly. (b) When the direction of entering the FOV is not known, end-effector is swept in a zigzag pattern.

images during the sweeping of the end-effector, the end-effector is considered to be present in the FOV.

2) Autofocus Adjustment: In the autofocus step, coarse and fine focus adjustments are conducted to focus on the end-effector tip. Coarse focus adjustment moves the focal plane in a large step size until the entire image produces a maximum focus measure value. In fine focus adjustment, a recursive quad-tree autofocusing method is used to accurately focus on the end-effector tip. After the coarse and fine focus adjustments, the in-focus end-effector tip is moved to the center of FOV through closed-loop visual servo control. This centering step is designed to reduce search time when switching to a higher magnification objective.

III. Methods

A. End-Effector Sweep Pattern

When an end-effector is initially mounted on the micromanipulator, the end-effector is often not within the FOV. However, the direction from which it will enter the FOV is usually known. Hence, our system moves the end-effector along this direction, and then, sweeps it perpendicularly [see Fig. 4(a)]. If the body of the end-effector instead of the tip enters the FOV, the system retracts the end-effector until the tip is found with the algorithm discussed in Section III-C. If the direction of entering the FOV is not known, the system moves the end-effector to the bottom left of the plane and sweeps it in a zigzag pattern [see Fig. 4(b)].

B. End-Effector Detection

When the end-effector is swept in the *X–Y* plane, the system uses a method based on an MHI to detect whether the end-effector has entered the FOV. The MHI-based detection is a view-based temporal method which is robust in representing movements and is employed in a variety of motion detection applications [14]. When the end-effector is out of

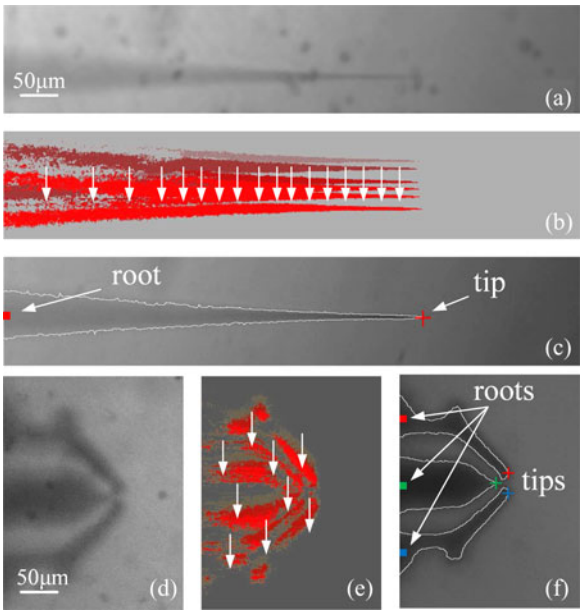

Fig. 5. Detection of end-effector. Arrows in (b) and (e) show the motion gradient of the moving end-effectors. (a) Original image of a micropipette. (b) Corresponding MHI of the moving micropipette. (c) Tip detection result based on active contour is shown in a background-removed image. (d) Original image of microgripper. (e) Corresponding MHI of the moving microgripper. (f) Tip detection result based on active contour is shown in a background-removed image.

focus, it appears blurry and the motion is not obvious to detect. Since the MHI-based method is able to enhance the motion representation by accumulating the end-effector's movement for a period of time, it is suitable to use to detect the subtle motion of the end-effector.

The original image is first denoised by using a Gaussian filter [15]. When the end-effector moves in the FOV, a silhouette image is obtained by subtracting two consecutive frames. The subtraction of two frames effectively suppresses the static noises from the background. The subtracted silhouette image is then binarized by applying a threshold to suppress background noise. When the end-effector moves, new silhouettes are captured and overlaid to the old silhouette that fades over time. The sequentially fading silhouettes record the motion history of the end-effector. Using this method, the MHI of the end-effector in the FOV is obtained [see Fig. 5(b) and (e)]. The sum of pixel value in the MHI is used as a measure to determine the presence of the end-effector. If the sum of pixel value is above a threshold (δ), the end-effector is considered to be present in the FOV. The threshold, δ, is calculated dynamically by analyzing 30 frames of the MHIs in which no end-effector is present.

$$\delta = \mu + a \cdot \sigma \tag{1}$$

where μ is the average of pixel value sum of the MHIs in which no end-effector is present, σ is the standard deviation, and a is a preset parameter which determines the threshold value. By adding several times of standards deviations (i.e., $a \cdot \sigma$) to the mean value, the threshold is able to reject most of the MHIs that do not have the presence of the end-effector. Accordingly, false positive detection caused by random noise and the shadow of end-effectors is reduced.

The movement direction of the end-effector, if not known, can be derived by computing the gradients of the MHI image. The gradients are obtained by applying a 3×3 Sobel gradient filter to the MHI image. If the detected overall motion gradient correlates with the sweep pattern, the end-effector is confirmed to be present in the FOV. The system then proceeds to the next step (contour detection). Otherwise, motion detection is regarded as a false positive case, and the system returns to the sweep step until the end-effector is correctly detected.

C. Contour Detection

Once the end-effector is detected to be present in the FOV, the end-effector's root and tip locations are estimated [see Fig. 5(c) and (f)]. In order to obtain a high estimation accuracy, the background is first removed by subtracting a background image from the current frame. The background image is recorded at the time when no end-effector is present in the FOV. The end-effector's contour is then detected by using the active contour method [16].

An active contour is a continuous spline defined by $\mathbf{v}(s) = (x(s), y(s))$, where x and y are image coordinates and $s \in [0, 1]$. The active contour deforms in the spatial domain of an image to minimize

$$E_{\text{snake}} = \int_0^1 E_{\text{int}}(\mathbf{v}(s)) + E_{\text{ext}}(\mathbf{v}(s))\, \mathrm{d}s \tag{2}$$

where E_{int} is the internal energy composed of the first and second derivatives of $\mathbf{v}(s)$, and E_{ext} is the external energy

$$E_{\text{ext}}(\mathbf{v}(s)) = -|\nabla(G_\sigma(x, y) * I(x, y))|^2 \tag{3}$$

where ∇ and $*$ are gradient and convolution operators, respectively, $G_\sigma(x, y)$ is a Gaussian filter with standard deviation σ, and $I(x, y)$ is the image data. The active contour model is initialized by detecting a rough contour of the last binarized silhouette image overlaid on the MHI. Then, the initial contour was deformed in the background-removed image under the influence of the internal and external forces.

With the detected contour of the end-effector [see Fig. 5(c) and (f)], the average position of the contour points on image boundaries is taken as the position of the root of the end-effector. The point with the largest Euclidean distance to the root location is considered the end-effector's tip position. For end-effectors with multiended tips (e.g., microgrippers), tip locations are detected separately.

D. Focus Assessment

In this step, the focal plane is adjusted to focus on the end-effector tip. The normalized variance method [17] is used to calculate the focus measure. It compensates for the differences in average image intensity (μ) among different images by normalizing the final output with the mean intensity [18]. The focus measure, F changes as the system adjusts the focal plane. When F reaches the global maximum, the end-effector is considered in focus.

$$F = \frac{1}{W \cdot H \cdot \mu} \sum_W \sum_H (I(x, y) - \mu)^2 \tag{4}$$

where W and H are the image width and height, respectively, $I(x, y)$ is the pixel intensity at the point (x, y), and μ is the average image intensity.

With the completion of the aforementioned coarse focusing step, fine focus adjustment updates the most in-focus region, R_f until the region contains the end-effector tip. R_f is a region with a predefined size $m \times n$ satisfying that the focus measure F of the region R_f is larger than any other region of the same size in the image.

The detection of R_f is performed by using a quad-tree recursive algorithm. The method recursively divides a region into four subregions with equal area. Out of the four subregions, the one with the highest focus measure F is further partitioned into four subregions. This procedure repeats recursively until the area of the subregion is equal or less than the area $m \times n$ of R_f. If the most in-focus region

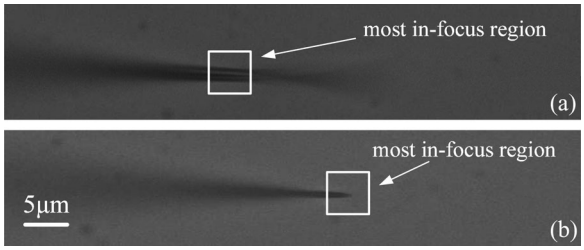

Fig. 6. Most in-focus region of the end-effector is detected by using a quad-tree recursive searching method. (a) Most in-focus region is detected to be on the end-effector body (not on the tip). (b) Tip is brought to focus (i.e., most in-focus region is now on the tip).

R_f is found to contain the end-effector body instead of the tip of the end-effector [see Fig. 6(a)], the focal plane is moved downwards since the end-effectors are always mounted at a tilting angle with tip side down in micromanipulation. The recursive detection of R_f and focal plane adjustment are then repeated until the end-effector tip is brought in focus [see Fig. 6(b)].

E. Centering End-Effector Tip

After the end-effector tip is brought in focus under a low-magnification objective, centering the tips is performed before the microscope switches to a higher magnification. By centering the tips under a low magnification, the end-effector is more likely to be present in the FOV when switching to a higher magnification. Experimentally, this step can significantly reduce the *X–Y* sweeping time required to locate the end-effector under higher magnifications. In our system, the in-focus end-effector tip is visually tracked and centered via closed-loop visual servo control.

Visual tracking algorithms can be classified into point tracking, kernel tracking, and silhouette tracking [19]. Representative algorithms were implemented in this study, and their performance was compared. In point tracking, the center point of the most in-focus region is detected and taken as the initial end-effector tip position. Since the end-effector was moved at a constant speed, the motion of end-effector tips was modeled as a constant velocity system. A Kalman filter is then applied to predict and optimize the end-effector tip position. In the kernel tracking category, template matching was tested to track end-effector tips. A template is manually captured, and the normalized cross correlation [20] of the template with real-time images is calculated as a measure to detect the end-effector's tip. Silhouette tracking is typically based on contour evolution and shape recognition. The active contour tracking approach was chosen and tested to detect the end-effector tip within a region of interest. For an end-effector with multiended tips, an average position of all tips was used as the overall tip position. Using the visually tracked tip position as feedback, an image-based PID visual servo controller was used to position the end-effector tip to the center of the FOV.

IV. Experimental Results

In the experiments, a micropipette (1 μm in tip diameter) and a microgripper were used as example end-effectors. The end-effectors were mounted along the *X*-axis with a tilting angle of 30° to the left side of the FOV. Before the automated procedure started, the end-effector tip was readily placed within the 4-mm cube workspace [see Fig. 2(a)] with unaided eyes, above the focal plane.

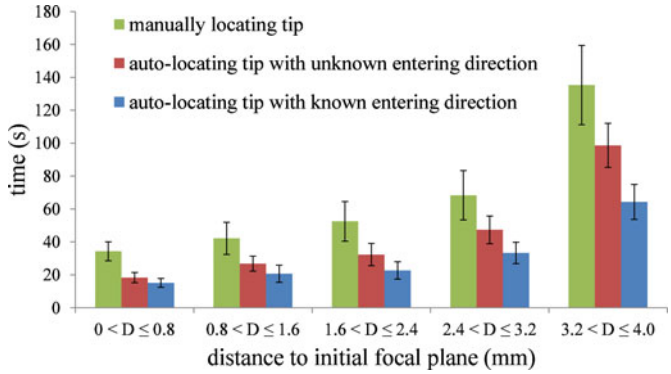

Fig. 7. Time of manually locating end-effector tip; autolocating end-effector tip with unknown and known entering direction. Within each group (distance to initial focus plane), $n = 20$ (ten trials to locate micropipette tip and ten trials to locate microgripper tips).

A. Overall Performance

The goal is to bring the end-effector tip to the center of the FOV under 4× magnification first, then under 10× magnification, and, finally, under 20× magnification. The experiments were categorized into five groups according to the end-effector's initial distance (D) to the bottom of the workspace [see Fig. 2(a)].

The experiments were first conducted using bright field imaging under two conditions: with known and unknown direction of the end-effector to enter the FOV. Fig. 7 summarizes the overall time spent on locating the end-effector and bringing its tip to the center of the FOV under 20× magnification. The average time of all five groups with unknown entering direction was 44.7 s, while the average time with known entering direction was only 31.2 s. These results demonstrate quantitatively that the overall locating time is significantly shorter ($p < 0.001$) by using the information of end-effector's entering direction.

The task of locating end-effector tips in the five groups was also conducted manually by three skilled micromanipulation operators. The results shown in Fig. 7 demonstrate that the overall time to autolocate end-effector tip, with or without known entering direction, is significantly shorter ($p < 0.001$) than in manual operation (averagely 64.8 s). In particular, in many micromanipulation tasks, end-effector's entering direction is known. With known entering direction, time required to autolocate the tip is shorter by over 50% compared with manual operation, throughout the five groups. In all groups of experiments, the deviations of time were caused by D value differences and the differences in initial lateral distance of the tip to the FOV.

We also experimented using only 4× and 20× magnifications in the locating experiments. After locating the end-effector tips under 4× magnification, the system directly switched to 20× (instead of 10×). The average time of 100 trials (under bright field imaging) using only 4× and 20× magnifications was 44.8 s (with known entering direction), which is much longer than the average time (31.2 s) of autolocating the tip by using 4×, 10×, and 20× magnifications sequentially. This is because the end-effector tip was sometimes out of the FOV when directly switching from 4× to 20×. When the tip was out of the FOV, the locating time was significantly lengthened because additional lateral sweeping and focus adjustments were needed under 20×. Experimental results also showed that the locating time under higher magnifications (i.e., 10×, 20×) is short (<5 s). This is because, after locating under the magnification of 4×, the end-effector tips are very close to the center of FOV. Accordingly, the searching time for end-effector tips is greatly reduced under higher magnifications.

TABLE I
EXPERIMENTAL RESULTS OF LOCATING END-EFFECTOR TIPS UNDER THREE IMAGING MODES

Imaging mode	Overall success rate	Success rate of detection step	Success rate of autofocus step	Average tracking error		
				Kalman filter (μm)	template matching (μm)	active contour (μm)
Bright field	97%	99%	98%	2.12	1.91	0.98
DIC	92%	94%	98%	2.01	1.87	1.34
Phase contrast	87%	98%	89%	2.53	1.82	3.07

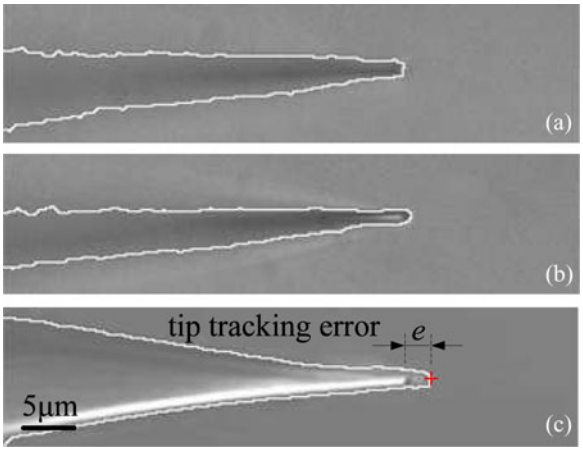

Fig. 8. Active contour detection under different imaging modes. (a) Bright field, (b) DIC, and (c) phase contrast.

TABLE II
EFFECT OF DIFFERENT THRESHOLD VALUES ON DETECTION TIME AND OVERALL SUCCESS RATE

Threshold (δ)	$\mu+1\sigma$	$\mu+3\sigma$	$\mu+6\sigma$	$\mu+9\sigma$
MHI detection time (s)	17.4	23.2	30.6	42.7
Overall success rate	87%	95%	98%	99%

Each data point in the table was from 100 trials, all under bright field imaging.

B. Performance Under Different Imaging Modes

The end-effector autolocating technique was then tested under three different imaging modes (100 trials for each imaging condition): bright field, DIC, and phase contrast. The experimental results are summarized in Table I.

Overall success rate refers to the rate of achieving the overall objective (locating and bringing the tip to the FOV of 20× magnification). The overall success rate under bright field imaging is higher than under DIC and phase contrast (97% versus 92% and 87%). This is because the depth of field of DIC imaging (2.6 μm for 20×) is smaller compared with bright field imaging (5.5 μm for 20×), and a halo is present around the end-effector tip under phase contrast [see Fig. 8(c)]. The smaller depth of field in DIC caused the end-effector not always to be detected between two focus levels. The halo in phase contrast caused the system to sometimes fail to correctly focus on the end-effector tip. Thus, the success rate in the autofocus step under phase contrast was significantly lower than the other two imaging modes (89% versus 98%).

The tracking algorithms based on the Kalman filter, template matching, and active contour were evaluated under the three imaging modes by calculating the average tip tracking error across 200 frames during tip centering. The tip tracking error summarized in Table I is the Euclidean distance between the detected tip location and the actual tip position [see Fig. 8(c)]. The average tip tracking errors for Kalman filter tracking and active contour tracking under phase contrast are the largest because of the halo around the tip which significantly influenced the focus assessment and reduced the contour detection accuracy. In contrast, there is no significant performance difference among the three imaging modes for the template matching algorithm.

The experimental results also show that the active contour method outperforms Kalman filter tracking and template matching in terms of average tracking error for bright field and DIC imaging. Optimal results for template matching are only possible when there is no significant changes in brightness and shadowing. Changes in scaling and rotation also can lead to false detection and loss of the tip position. Additionally, users may change end-effectors during a micromanipulation task. The slightly different shapes/dimensions across end-effectors of the same type can render template matching ineffective. Regarding Kalman filter tracking, it heavily relies on the result from the focus assessment step. However, the center point of the most in-focus region is not always the same as the end-effector tip location. In summary, the results demonstrate that active contour tracking under the bright field imaging mode was the most effective to locate end-effectors under microscopy.

C. Discussion

In the experiments for locating micropipettes under bright field imaging, 3 out of 100 trials failed. The three failure cases were caused by improper selections of the threshold value [δ in (1)] in MHI detection. To investigate the effect of threshold value selection on MHI detection, four groups of experiments were conducted with different threshold values. Table II summarizes the results from using different δ values.

When δ is set too low, the shadow of the micropipette body is detected by the MHI algorithm much earlier than the body itself. When this occurs, the active contour algorithm forms a contour around the shadow, and then, the recursive autofocusing algorithm locates a most-in-focus location on the shadow after the coarse focus adjustment. When the system lowers the focal plane in order to focus on the micropipette tip, the most-in-focus location on the shadow stays unchanged (because the shadow and the micropipette body are too far apart). In some cases with too low a δ value set, the system was not able to locate the micropipette tip even after reaching the motion limit of microscope focus.

On the other hand, when the threshold value, δ is set too high, it takes much longer for MHI detection to complete although the overall success rate in locating the end-effector tip is higher [see Table II]. A balance of MHI detection time and the overall success rate must be considered in practice.

In the microgripper experiments under bright field imaging, 5 out of 100 trials failed. Two failure cases were also caused by improper selection of the threshold for MHI detection. Other failure cases occurred in the group of experiments for locating microgripper tips assuming

Fig. 9. Autolocating microgripper tips failed due to other structures appeared in the FOV first.

unknown entering direction, where other structures (rather than the gripping tips) appeared in the FOV first, as shown in Fig. 9. Hence, at the completion of the autolocating process, the first present structure was considered the microgripper tip and brought to the center of the FOV. This problem can be avoided in practice since the microgripper's entering direction is typically known in a given micromanipulation system configuration.

Based on the experimental results and observations, we attempt to establish a set of guidelines to implement the technique to autolocate an end-effector in micromanipulation. First, the threshold value in MHI detection must be properly selected, with a balance of failure rates and time taken. Second, the threshold value selection is also sensitive to lighting. Histogram analysis in our experiments confirmed that an average value of pixel intensity, between 80 and 150, in the initial background image should be used to mitigate the effect of lighting variations on MHI detection. This can be readily implemented in a control program to properly set lighting intensity in a micromanipulation system. Third, the task of autolocating end-effector tips should be conducted under bright field imaging (versus DIC or phase contrast). Fourth, The autolocating sequence should be performed under gradually increasing magnifications (e.g., $4\times$, $10\times$, and $20\times$) rather than under abrupt magnification changes (e.g., $4\times$, and then, immediately $20\times$).

V. Conclusion

This paper presented a technique to automatically locate an end-effector under microscopy imaging. Locating the end-effector tip is the very first step in either manual or automated micromanipulation. The technique described in this paper is capable of searching for out-of-FOV, out-of-focus, and low contrast end-effectors. Experimental results demonstrate that the search time can be reduced by over 50% with the automated technique. The overall success rate of the locating system is 97% under the bright field imaging mode. Based on the experimental results and observations, the following guidelines are established to implement the technique of autolocating end-effector tips in order to achieve a high efficiency and success rate.

1) The threshold value in MHI detection must be properly set ($[\mu + 3\sigma, \mu + 6\sigma]$).
2) Lighting intensity must be properly set, for instance, with the average value of pixel intensity in the initial background image set between 80 and 150.
3) Bright field imaging should be chosen (versus DIC and phase contrast) in the autolocating process.
4) The active contour algorithm is most effective under bright field imaging to detect and track end-effector tips.
5) Abrupt magnification change should be avoided when switching from a low to a high magnification.
6) The prior knowledge of end-effector entering direction improves both completion time and the overall success rate.

References

[1] T. Fukuda, M. Nakajima, M. Ahmad, Y. Shen, and M. Kojima, "Micro- and nanomechatronics," *IEEE Ind. Electron. Mag.*, vol. 4, no. 4, pp. 13–22, Dec. 2010.
[2] B. K. Chen, Y. Zhang, and Y. Sun, "Active release of microobjects using a MEMS microgripper to overcome adhesion forces," *J. Microelectromech. Syst.*, vol. 18, no. 3, pp. 652–659, Jun. 2009.
[3] F. Beyeler, S. Member, A. Neild, S. Oberti, D. J. Bell, Y. Sun, J. Dual, and B. J. Nelson, "Monolithically fabricated microgripper with integrated force sensor for manipulating microobjects and biological cells aligned in an ultrasonic field," *J. Microelectromech. Syst.*, vol. 16, no. 1, pp. 7–15, 2007.
[4] D. O. Popa and H. E. Stephanou, "Micro and meso scale robotic assembly," *J. Manuf. Process.*, vol. 6, no. 1, pp. 52–71, Jan. 2004.
[5] M. Sitti, "Microscale and nanoscale robotics systems," *IEEE Robot. Autom. Mag.*, vol. 14, no. 1, pp. 53–60, Mar. 2007.
[6] Z. NI, A. Bolopion, J. Agnus, R. Benosman, and S. Regnier, "Asynchronous event-based visual shape tracking for stable haptic feedback in microrobotics," *IEEE Trans. Robot.*, vol. 28, no. 5, pp. 1081–1089, Oct. 2012.
[7] Y. H. Anis, J. K. Mills, and W. L. Cleghorn, "Vision-based measurement of microassembly forces," *J. Micromech. Microeng.*, vol. 16, no. 8, pp. 1639–1652, Aug. 2006.
[8] B. Tamadazte, N. L.-F. Piat, and S. Dembele, "Robotic micromanipulation and microassembly using monoview and multiscale visual servoing," *IEEE/ASME Trans. Mechatron.*, vol. 16, no. 2, pp. 277–287, Apr. 2011.
[9] T. Kasaya, H. T. Miyazaki, S. Saito, K. Koyano, T. Yamaura, and T. Sato, "Image-based autonomous micromanipulation system for arrangement of spheres in a scanning electron microscope," *Rev. Sci. Instrum.*, vol. 75, no. 6, pp. 2033–2042, 2004.
[10] H. Kuba, K. Hotta, and H. Takahashi, "Automatic particle detection and counting by one-class SVM from microscope Image," in *Advances in Neuro-Information Processing*, G. Köppen, Mario, Kasabov, Nikola, and Coghill, Eds. Berlin, Germany: Springer-Verlag, 2009, pp. 361–368.
[11] S. Yi, D. Labate, G. R. Easley, and H. Krim, "A shearlet approach to edge analysis and detection," *IEEE Trans. Image Process*, vol. 18, no. 5, pp. 929–941, May 2009.
[12] J. Liu, C. Leung, Z. Lu, and Y. Sun, "Quantitative analysis of locomotive behavior of human sperm head and tail," *IEEE Trans. Biomed. Eng.*, vol. 60, no. 2, pp. 390–396, Feb. 2013.
[13] J. Liu, Z. Gong, K. Tang, Z. Lu, and Y. Sun, "Locating end-effector tips in automated micromanipulation," presented at the IEEE Int. Conf. Robotics and Automation, Karlsruhe, Germany, 2013.
[14] M. A. R. Ahad, J. K. Tan, H. Kim, and S. Ishikawa, "Motion history image: Its variants and applications," *Mach. Vis. Appl.*, vol. 23, no. 2, pp. 255–281, Oct. 2010.
[15] E. R. Davies, *Machine Vision: Theory, Algorithms, Practicalities*, 3rd ed. San Francisco, CA, USA: Morgan Kaufmann, 2004.
[16] M. Kass, A. Witkin, and D. Terzopoulos, "Snakes: Active contour models," *Int. J. Comput. Vis.*, vol. 1, no. 4, pp. 321–331, 1988.
[17] T. Yeo, S. Ong, and R. Sinniah, "Autofocusing for tissue microscopy," *Image Vis. Comput.*, vol. 11, no. 10, pp. 629–639, Dec. 1993.
[18] Y. Sun, S. Duthaler, and B. J. Nelson, "Autofocusing in computer microscopy: Selecting the optimal focus algorithm," *Microsc. Res. Techn.*, vol. 65, no. 3, pp. 139–49, Oct. 2004.
[19] A. Yilmaz, O. Javed, and M. Shah, "Object tracking: A survey," *ACM Comput. Surv.*, vol. 38, no. 4, pp. 1–45, Dec. 2006.
[20] Z. Yang, "Fast template matching based on normalized cross correlation with centroid bounding," in *Proc. Int. Conf. Meas. Technol. Mechatron. Autom.*, Mar. 2010, vol. 2, no. 1, pp. 224–227.